Dimensionality-dependent type-II Weyl semimetal state in $Mo_{0.25}W_{0.75}Te_2$

Peiling Li,[1,*] Ya Deng,[2,*] Chuang-Han Hsu,[3] Chao Zhu,[2] Jian Cui,[4] Xue Yang,[1,5] Jiadong Zhou,[2] Yi-Chun Hung,[3] Jie Fan,[1,6] Zhongqing Ji,[1,6] Fanming Qu,[1,5,6] Jie Shen,[1] Changli Yang,[1] Xiunian Jing,[1,6] Hsin Lin,[3] Zheng Liu,[2,†] Li Lu,[1,4,5,6,‡] and Guangtong Liu[1,5,6,§]

[1]*Beijing National Laboratory for Condensed Matter Physics, Institute of Physics, Chinese Academy of Sciences, Beijing 100190, China*
[2]*School of Materials Science and Engineering, Nanyang Technological University, Singapore 639798, Singapore*
[3]*Institute of Physics, Academia Sinica, Taipei 115229, Taiwan*
[4]*Beijing Academy of Quantum Information Sciences, Beijing 100193, China*
[5]*University of Chinese Academy of Sciences, Beijing 100049, China*
[6]*Songshan Lake Materials Laboratory, Dongguan, Guangdong 523808, China*

(Received 17 February 2021; revised 6 August 2021; accepted 9 August 2021; published 23 August 2021)

Weyl nodes and Fermi arcs in type-II Weyl semimetals (WSMs) have led to lots of exotic transport phenomena. Recently, $Mo_{0.25}W_{0.75}Te_2$ has been established as a type-II WSM with Weyl points located near Fermi level, which offers an opportunity to study its intriguing band structure by electrical transport measurements. Here, by selecting a special sample with the thickness gradient across two- (2D) and three-dimensional (3D) regimes, we show strong evidence that $Mo_{0.25}W_{0.75}Te_2$ is a type-II Weyl semimetal by observing the following two dimensionality-dependent transport features: (1) a chiral-anomaly-induced anisotropic magnetoconductivity enhancement, proportional to the square of in-plane magnetic field (B_{in}^2); and (2) an additional quantum oscillation with thickness-dependent phase shift. Our theoretical calculations show that the observed quantum oscillation originates from a Weyl-orbit-like scenario due to the unique band structure of $Mo_{0.25}W_{0.75}Te_2$. The *in situ* dimensionality-tuned transport experiment offers an alternative strategy to search for type-II WSMs.

DOI: 10.1103/PhysRevB.104.085423

I. INTRODUCTION

As a new state of matter, Weyl semimetals (WSMs) [1–3] have aroused intense interest in condensed matter physics. Together with the first WSM that was experimentally discovered in TaAs, a range of novel topological properties [4–9] have been revealed, such as symmetry protected band crossing points known as Weyl nodes [4–7], topological surface states known as Fermi arcs [4–7], and anisotropic negative magnetoresistance (MR) induced by chiral anomaly [8–11]. Different from type-I WSMs with a pointlike Fermi surface at Weyl nodes, type-II WSMs [12–14] with tilted Weyl cones break the stringent Lorentz symmetry and exhibit lots of exotic transport properties such as Klein tunneling [15]. Recently, the $Mo_xW_{1-x}Te_2$ system has been experimentally confirmed as a type-II WSM [16–20]. Among them, our previous angle-resolved photoemission spectroscopy (ARPES) results and band structure calculations [20] have shown that $Mo_{0.25}W_{0.75}Te_2$ has larger topological Fermi arcs compared with WTe_2. More importantly, the Fermi energy is found to be very close to Weyl nodes [20], which makes $Mo_{0.25}W_{0.75}Te_2$ an ideal platform to observe peculiar transport properties arising from emergent Weyl fermions and corresponding topological surface states.

Chiral anomaly and Weyl orbit are two characters of WSMs that researchers pursue in transport measurements. At present, chiral anomaly is the widely adopted method [8,9,16,17] to confirm WSM states by detecting anisotropic negative MR. However, the negative MR could possibly be induced by other mechanisms [21–24]. For Weyl orbits, the convincing transport feature is to probe an additional quantum oscillation with thickness-dependent phase shift [17,25–27]. However, to conduct such thickness-dependent experiments, it remains challenging to control material parameters such as defects and compositions in different mechanically exfoliated sample batches. Therefore, more efforts should be made to get convincing evidences of WSM states via transport measurements. Theoretically [28,29], a WSM state only exists in three-dimensional (3D) samples, as two-dimensional (2D) thin samples inevitably open a gap at Weyl points and destroy the WSM state. This means that WSM states will degrade in a thinner sample. Hence, *in situ* dimensionality-dependent magnetotransport experiments are necessary to verify WSM states, which allows us to investigate chiral anomaly and Weyl orbit in a single device with thickness gradient.

Here, we consider a $Mo_{0.25}W_{0.75}Te_2$ sample with thickness gradient along the *a* axis parallel to the zigzag chain of W (or Mo). Combining low-temperature magnetotransport measurements and theoretical calculations, we demonstrate that $Mo_{0.25}W_{0.75}Te_2$ is a type-II WSM with unique surface states by observing dimensionality-dependent anisotropic negative

*These authors contributed equally to this work.
†Author to whom correspondence should be addressed: z.liu@ntu.edu.sg
‡lilu@iphy.ac.cn
§gtliu@iphy.ac.cn

MR and an additional quantum oscillation frequency with thickness-dependent phase shift. Our theoretical calculations suggest that this quantum oscillation is likely resulting from a scenario mimic of the Weyl orbit. Moreover, the disappearance of these two characteristics in the thinner samples is consistent with our theoretical calculations. Our results contribute to a better understanding of the peculiar transport phenomena in topological WSMs.

II. RESULTS

The $Mo_{0.25}W_{0.75}Te_2$ flakes were synthesized by the molten-salt assisted chemical vapor deposition (CVD) method [30]. More information about the sample is detailed in the Supplemental Material [31]. Figures 1(a) and 1(b) show the room-temperature atomic configuration and optical image of synthesized $1T'$ $Mo_{0.25}W_{0.75}Te_2$ flakes. The $1T'$ structure is determined by the annular dark-field scanning transmission electron microscopy (ADF-STEM) image in Supplemental Material Fig. S1, and the Mo-doping concentration is estimated to be around 0.2. The x-ray photoelectron spectroscopy (XPS) wide scan spectrum shown in Fig. S2 confirms the coexistence of Mo, W, and Te [32,33]. This result is also supported by the Raman spectrum (see Fig. S3) where the vibration modes of $1T'$ -WTe_2 and $MoTe_2$ coexist in the Raman spectrum of $Mo_{0.25}W_{0.75}Te_2$ [32,34]. Furthermore, the peak intensity calculation from the XPS spectrum in Fig. 1(c) indicates the composition of the synthesized alloy is stoichiometric $Mo_{0.25}W_{0.75}Te_2$. The energy-dispersive x-ray spectroscopy (EDX) shown in Fig. 1(d) reveals the high quality of synthesized material by observing the uniform distribution of Mo, W, and Te atoms.

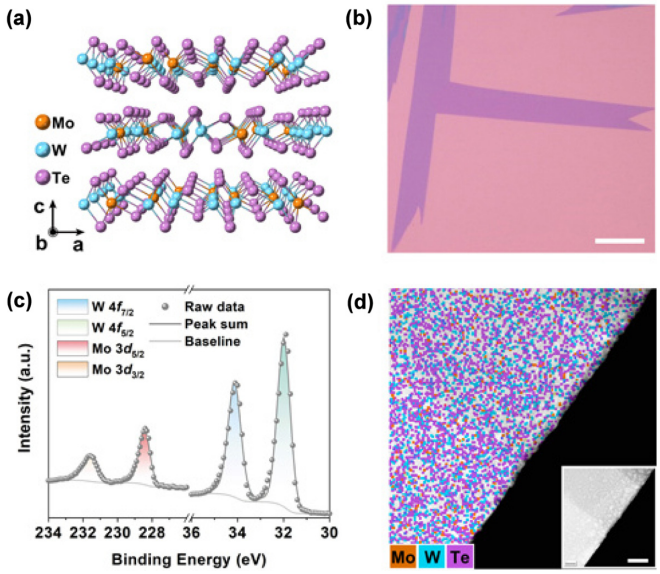

FIG. 1. Characterization of synthesized $Mo_{0.25}W_{0.75}Te_2$ flakes. (a), (b) Atomic configuration and optical image of synthesized $Mo_{0.25}W_{0.75}Te_2$ flakes. (c) The high-resolution x-ray photoelectron spectroscopy (XPS) spectrum of as-synthesized $Mo_{0.25}W_{0.75}Te_2$ flakes. The peak calculation results reveal that the composition of the synthesized alloy is stoichiometric $Mo_{0.25}W_{0.75}Te_2$. (d) The elemental energy-dispersive x-ray spectrometry (EDX) mapping of $Mo_{0.25}W_{0.75}Te_2$ flakes collected from the region are shown in the inserted TEM image, revealing a uniform distribution of constituent atoms. The scale bars in (b) and (d) are 20 μm and 100 nm, respectively.

As mentioned above, $Mo_{0.25}W_{0.75}Te_2$ is an ideal platform for transport study on type-II WSMs. Previous studies [35,36] have shown that a structural phase transition from the $1T'$ to T_d phase occurs at low temperatures, which breaks the inversion symmetry and allows a type-II WSM state to emerge. Hence, we carried out low-temperature magneto-transport experiments on high-quality $Mo_{0.25}W_{0.75}Te_2$ flakes. Most importantly, the studied sample has a thickness gradient ranging from 6 to 32 nm (see Fig. S4). Compared to the bulk electron and hole mean free path $l_e \sim 29$ nm and $l_h \sim 24$ nm (see Supplemental Material Table S2 [31]) and our band structure calculation (see Sec. I of the Supplemental Material [31]), the sample has both 2D-like and 3D-like transport properties. Meanwhile, the same sample guarantees that different segments have the same composition, which offers us an ideal platform to examine the exotic transport properties of a WSM in different dimensionalities. Weyl points were theoretically proposed to only exist in bulk materials [28,29], which means WSM states degrade with the sample thinned down. Thus, we can study the dimensionality effect on WSM states by simultaneously measuring the low-temperature magneto-transport properties at different segments with a thickness of L nm (hereafter named Seg-L). The upper inset of Fig. 2(a) displays the temperature dependence of zero-field longitudinal resistivity $\rho_{xx}(T)$, from which one notices that Seg-28 exhibits a metallic conducting behavior. In contrast, Seg-8 shows a semiconducting behavior [upper inset of Fig. 2(d)], which is found to obey the 2D Mott's variable range hopping [37,38] mechanism of the conduction (see Fig. S5). Upon applying a perpendicular magnetic field to the sample, Seg-28 displays a nonsaturated parabolic magnetoresistivity (MR $= \frac{\rho_{xx}(B)-\rho_{xx}(0)}{\rho_{xx}(0)} \times 100\%$) of $\sim$300% at 14 T and 0.3 K [Fig. 2(a)], which agrees well with previous observations for bulk WTe_2 [39], indicating its 3D nature. The small dome-shaped MR around zero magnetic field below $T = 4$ K is ascribed to electron-electron interactions (EEIs) [40–42] as shown below. Compared with Seg-28, Seg-8 shows a small positive MR of 20% [Fig. 2(d)]. At small magnetic fields, the steep rise of MR arises from the weak antilocalization, signifying the strong spin-orbit interaction (SOI) in the present system [16,42]. The oscillatory component superimposed on MR at high fields in Figs. 2(a) and 2(d) corresponds to quantum oscillations.

For a type-II WSM, the chiral-anomaly-induced negative longitudinal MR [16,17] is expected when the applied electric (E) and magnetic fields (B) are aligned to the tilt direction of Weyl cones. Figures 2(b) and 2(e) show in-plane magnetic field experimental results, where the field is applied along the a axis of sample ($B \| E \| a$). As expected, a clear negative longitudinal MR is observed in Seg-28 in the whole measured field ranging from -14 T to 14 T. With increasing temperature, the negative MR progressively weakens and disappears around $T = 10$ K. In stark contrast to negative MR in Seg-28, Seg-8 only shows positive MR. To check if the observed negative MR is induced by chiral anomaly, *in situ* tilt experiments are performed at $T = 0.3$ K. The data shown in Fig. 2(c) illustrate that of Seg-28 are very sensitive to the tilt angle (θ). The negative MR only occurs when $\theta \geqslant 75^\circ$ and reaches

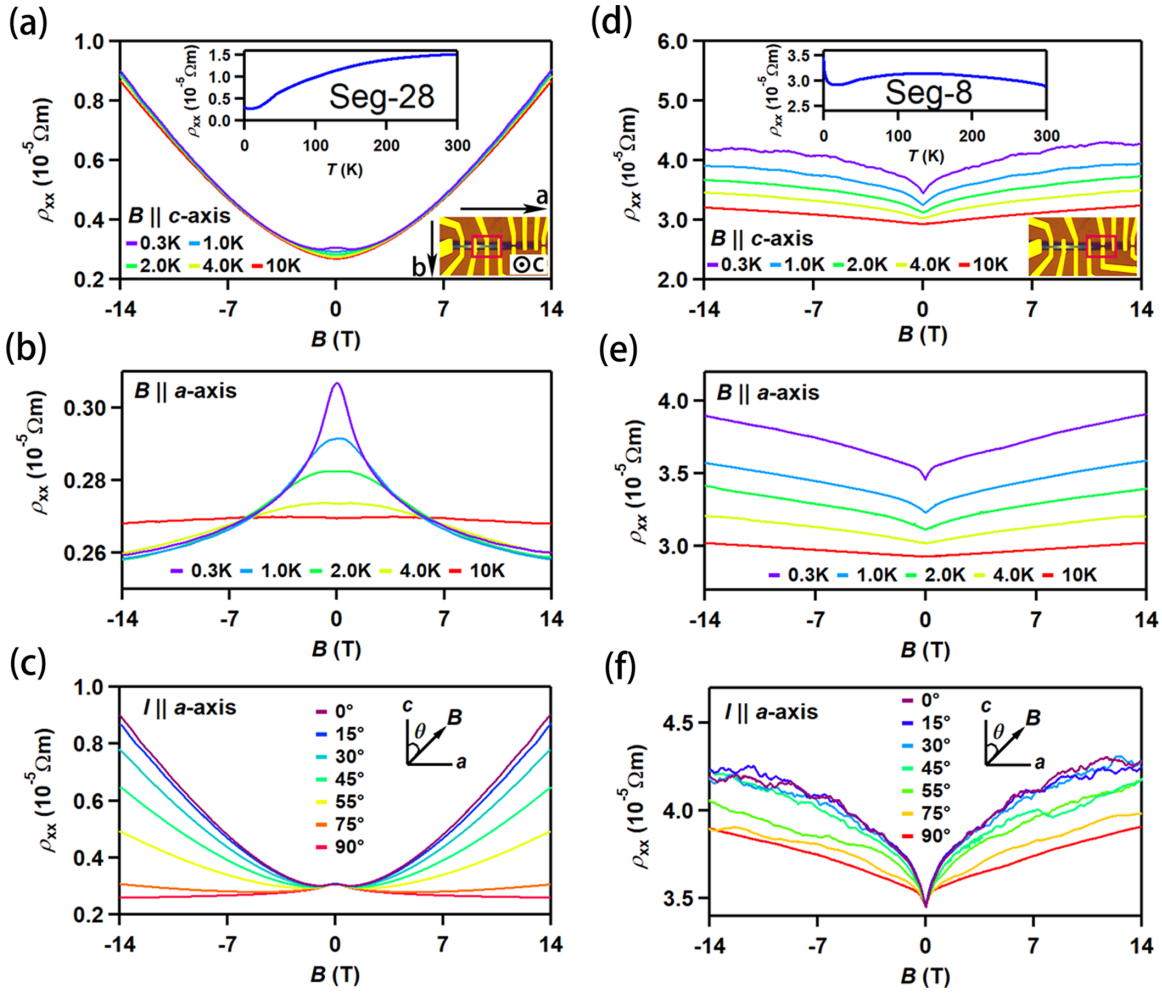

FIG. 2. Dimensionality-dependent magnetotransport characterization of the as-synthesized $Mo_{0.25}W_{0.75}Te_2$ sample. (a), (d) Longitudinal magnetoresistivity ρ_{xx} of Seg-28 and Seg-8 in perpendicular magnetic field, respectively. The upper inset of (a) and (d) plots the zero-field resistivity of Seg-28 and Seg-8 as a function of temperatures. The region marked with a solid red line in the lower right inset of (a) and (d) is the optical image of Seg-28 and Seg-8 with the sample thickness of 28 and 8 nm. (b), (e) Longitudinal magnetoresistivity ρ_{xx} of Seg-28 and Seg-8 in parallel magnetic field, respectively. (c), (f) Magnetic field dependence of longitudinal magnetoresistivity ρ_{xx} of Seg-28 and Seg-8 at $T = 0.3$ K with different tilt angles θ. The inset is a schematic drawing of the tilt experimental setup, where a and c represents the crystallographic axis, and θ is the tilt angle between the magnetic field B and the positive direction of the c axis.

a maximum at $\theta = 90^\circ$ ($B \| E \| a$). We note that the observed highly anisotropic longitudinal MR can be ascribed to the anisotropic Fermi surface [17,43], since the closed orbits of hole pockets in perpendicular magnetic field transform to open orbits in parallel field, which breaks the compensation of electron and hole [43]. However, the negative longitudinal MR in parallel field is a strong transport signature of chiral anomaly [8,9,16,17], which supports the existence of WSM states in Seg-28. Note that at small magnetic fields ($|B| < 1$ T), $\rho_{xx}(B)$ exhibits a tilt-angle independent behavior, which can be understood by the following EEI effect [40,41] analysis. Different from Seg-28, Seg-8 displays only positive MR at all tilt angles, as shown in Fig. 2(f). From the data presented above, we find that Seg-28 and Seg-8 exhibit distinct magnetotransport behaviors. This is closely related to their thicknesses, which can be interpreted as degradation of WSM states in a 2D-like region (see Sec. I and Fig. S6 of the Supplemental Material [31]).

To further demonstrate chiral anomaly in $Mo_{0.25}W_{0.75}Te_2$, we perform a quantitative analysis of low-temperature magnetotransport properties and present them in Fig. 3. From Fig. 3(a), we find that the zero-field resistivity $\rho_{xx}(0, T)$ from 22 to 10 K can be well fitted by $\rho_{xx}(0, T) \propto T^3$, which is attributed to *s-d* electron scattering [44]. Below $T = 10$ K, an upturn appears in the $\rho_{xx}(0, T)$ curve in Fig. 3(a), which can be described by the EEI mechanism as demonstrated below. Considering the EEI contribution [40–42,45,46] in the 2D case, the conductivity of a WSM can be expressed as

$$\sigma_{\mathrm{EEI}}(B, T) = \sigma_{\mathrm{D}} - \frac{e^2 c}{8\pi^2 \hbar} \tilde{F}\left[\ln\left(\frac{k_{\mathrm{B}} T \tau}{\hbar}\right) - \mathrm{g}_2(h)\right], \quad (1)$$

where $h = g\mu_{\mathrm{B}} B / k_{\mathrm{B}} T$, $\mathrm{g}_2(h)$ has two asymptotic forms with $\mathrm{g}_2(h) = 0.084h^2$ ($h \ll 1$), and $\mathrm{g}_2(h) = \ln(h/1.3)$ ($h \gg 1$) (see Sec. II of the Supplemental Material [31] for details). At

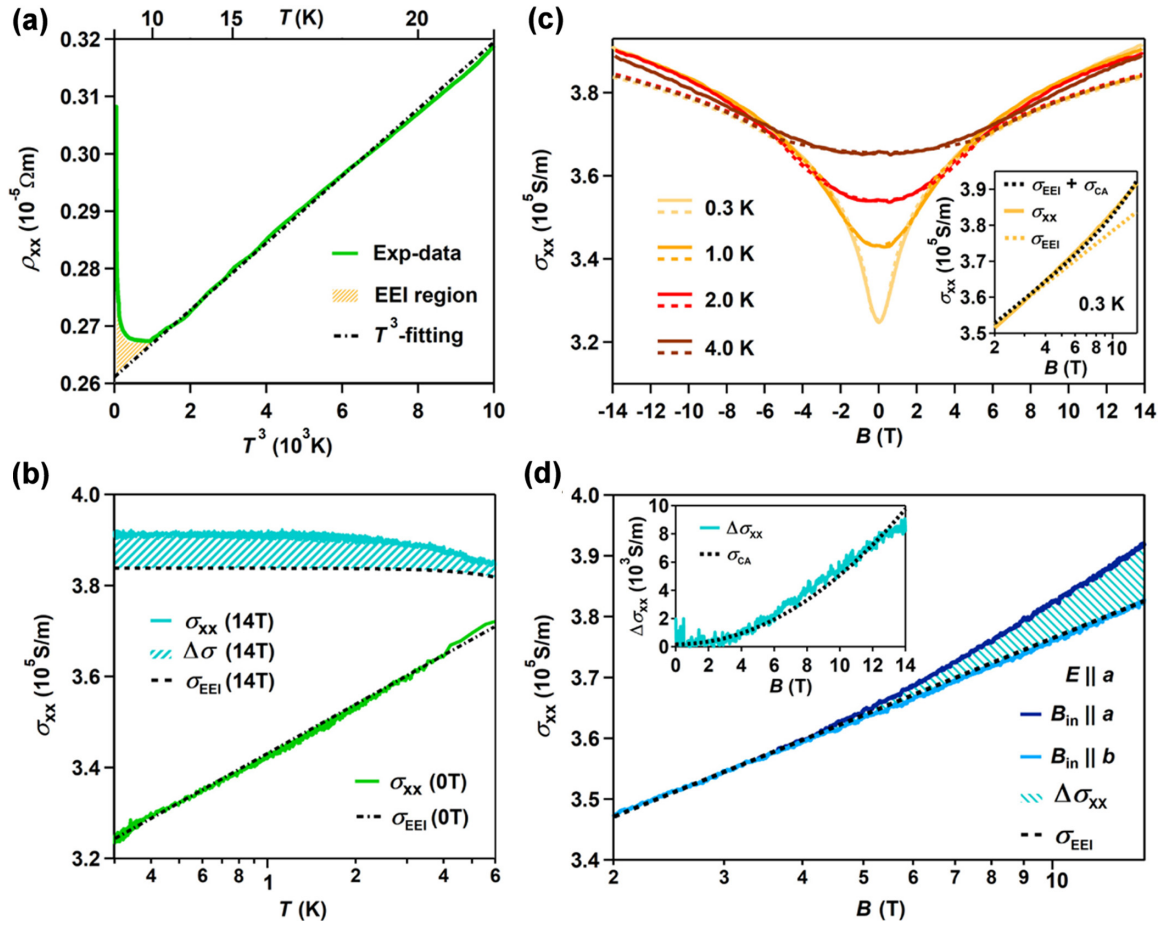

FIG. 3. Chiral-anomaly-induced magnetoconductivity enhancement in Seg-28. (a) The zero-field longitudinal resistivity versus T^3. The black dotted line represents the T^3-fitting curve, and the yellow shaded region indicates the EEI-induced resistivity upturn. (b) Signature of chiral-anomaly-induced magnetoconductivity enhancement. The solid blue and green lines are the temperature dependence of magnetoconductivity measured at 14 and 0 T in-plane magnetic fields, respectively. The dashed and dotted lines are theoretical curves calculated with Eqs. (1) and (2), respectively. (c) Magnetic field dependence of the in-plane σ_{xx} collected at selected temperatures. The dashed lines are the corresponding theoretical curves calculated with Eq. (1). The inset shows the magnetic field dependence of the in-plane σ_{xx} measured at 0.3 K in a semilogarithmic scale. The black and yellow dashed lines represent the theoretical curves calculated with Eq. (5) with and without consideration of chiral anomaly contribution, respectively. (d) Magnetoconductivities measured with the in-plane magnetic field parallel ($B_{in} \parallel a$) and perpendicular ($B_{in} \parallel b$) to the current direction. The dashed line represents the fitting results of Eq. (1). The inset shows the magnetoconductivity difference between these two magnetic field directions. The agreement between the experimental data and the theoretical curve calculated with Eq. (4) suggests that the magnetoconductivity enhancement is due to chiral anomaly.

zero field, Eq. (1) reduces to

$$\sigma_{\mathrm{EEI}}(0,T) = \sigma_{\mathrm{D}} - \frac{c}{4}\tilde{F}\frac{e^2 \ln(k_{\mathrm{B}}T\tau/\hbar)}{2\pi^2\hbar} \tag{2}$$

In Fig. 3(b), we plot $\sigma_{xx}(0\,\mathrm{T})$ as a function of temperature in a semilogarithmic scale. It is found that the experimental data can be well fitted by Eq. (2), confirming the low-temperature resistivity upturn arises from the EEI effect. Note that the EEI correction to the conductivity is two-dimensional, which indicates that the EEI is mainly contributed by surface states.

Now we turn to discuss one of our most important findings—chiral-anomaly-induced magnetoconductivity enhancement σ_{CA} under in-plane magnetic field ($B \| E \| a$). As shown above, the EEI also contributes a magnetoconductivity σ_{EEI}. We therefore need to remove the EEI contributions from the in-plane magnetoconductivity σ_{xx}. From Fig. 3(c), one can see that σ_{xx} can be well fitted by Eq. (1) at the low-field limit ($h \ll 1$), signifying that the low-field σ_{xx} is mainly contributed by the EEI. However, at a high-field limit ($h \gg 1$), a large discrepancy between the theoretical curves (dashed lines) and the experimental data (solid lines) indicates that there are additional contributions to σ_{xx}. To see it more clearly, we plot the experimental data of $\sigma_{xx}(14\,\mathrm{T})$ (solid blue line) and the EEI-contributed conductivity $\sigma_{EEI}(14\,\mathrm{T})$ (black dashed line) calculated with Eq. (1) in Fig. 3(b). It can be seen that the high-field conductivity $\sigma_{xx}(14\,\mathrm{T})$ shows an obvious enhancement compared to $\sigma_{EEI}(14\,\mathrm{T})$, highlighted by the blue shaded region. To find out the enhancement mechanism of σ_{xx}, we analyze the experimental data with the following model by considering the contributions of both the EEI and chiral anomaly,

$$\sigma_{xx} = \sigma_{\mathrm{EEI}} + \sigma_{\mathrm{CA}}. \tag{3}$$

According to literatures [8,9,16], σ_{CA} is proportional to B^2,

$$\sigma_{\mathrm{CA}} = C_{\mathrm{w}}B^2, \tag{4}$$

where $C_w = N\frac{e^4 v_F^3 \tau'}{4\pi^2 \hbar \Delta E^2}$ is the chiral anomaly coefficient, N is the pair number of Weyl points contributing to the conductivity, v_F is Fermi velocity, τ' is the axial relaxation time which can be approximately treated as intervalley scattering time τ_i [47], and ΔE is the chemical potential measured from the energy of Weyl points. We fit our experimental data with Eq. (3) and plot them in the inset of Fig. 3(c). The excellent agreement between the experimental data (solid yellow line) and the fitting curve (black dashed line) strongly suggests that the conductivity enhancement originates from chiral anomaly.

For a WSM, an anisotropic magnetotransport behavior originated from chiral anomaly is expected. It means that only when the external magnetic field is applied parallel to the electric field [8–11,16,17], an enhanced magnetoconductivity can be observed. Accordingly, we performed an in-plane tilt experiment to further confirm our argument. Figure 3(d) presents magnetoconductivities measured with the in-plane magnetic field parallel ($B_{in} \parallel a$) and perpendicular ($B_{in} \parallel b$) to the current direction. Indeed, the conductivity of the former case ($B_{in} \parallel E \parallel a$) is notably larger than the latter one. Moreover, we find that the conductivity of the latter case (light-blue line) can be nicely fitted by Eq. (1) (black dashed line), proving that it is completely contributed by the EEI. Here, we consider isotropic EEI contribution in the a and b axes (see Sec. VII and Fig. S10 of the Supplemental Material [31]), which is correct for the case that the g factor is almost equal in the ab plane [40,41].To quantitatively analyze the conductivity enhancement, in the inset of Fig. 3(d), we plot the conductivity difference $\Delta\sigma_{xx}$ between the two directions. We find it can be well described by Eq. (4), confirming that the magnetoconductivity enhancement is due to chiral anomaly. Additionally, we find that $C_w = 48.7\ T^{-2}$ S extracted from the experimental data is consistent with 44.1 T^{-2} S obtained via multicarrier fitting (see Sec. III and Fig. S7 of the Supplemental Material [31]) and 42.8 T^{-2} S calculated from $N\frac{e^4 v_F^3 \tau'}{4\pi^2 \hbar \Delta E^2}$ with $N = 4$ (see Table S2). This proves that the chiral-anomaly transport involves four pairs of Weyl points, which is in accordance with our previous ARPES results [20]. From the above analysis based on the temperature and tilt-angle dependence of magnetoconductivity, we conclude that low-temperature conductivity enhancement originates from chiral anomaly.

Next, we move to another significant finding in our experiments—a new kind of Weyl orbit. The recent theory [26,27] and experiment [17,25,48–51] have shown that Weyl orbit can be formed by connecting surface Fermi arcs and the zeroth bulk Landau levels, which we call conventional Weyl orbit and will lead to an additional quantum oscillation in MR curves. Moreover, the new quantum oscillation exhibits a unique thickness and tilt-angle-dependent phase shift. Theoretically, the nth peak position of the new quantum oscillation from Weyl orbit is predicted to be [27]

$$\frac{1}{B_n} = \frac{2\pi e}{\hbar S_k}\left[(n+\gamma)\cos\theta - \frac{L}{2\pi}\left(\vec{k}_w \cdot \hat{B} + 2\frac{\mu}{v_\parallel}\right)\right], \quad (5)$$

where n is the Landau level index, S_k is the area of enclosed cyclotron orbits in k space, γ is related to Berry phase, θ is the tilt angle between B and the c axis, L is the sample thickness, $\vec{k}_w \cdot \hat{B}$ is the separation of Weyl nodes along the direction of B, μ is the chemical potential, and $v_\parallel$ is the Fermi velocity parallel to B. In our experiments, however, we find a quantum oscillation with a large k space area S_k (shown below), which cannot be explained by the small Fermi arcs predicted earlier [19]. Alternatively, our theoretical calculations suggest that a similar quantum oscillation could be supported by the unique band structure of $Mo_{0.25}W_{0.75}Te_2$ rather than the conventional Weyl orbit [see Figs. 4(a) and 4(b) for the comparison]. As shown in Fig. 4(c) for 30-layer $Mo_{0.25}W_{0.75}Te_2$, the Weyl-orbit-like (WOL) orbit is composed of the surface states near the electron pocket (S_{t2}) of the top surface and the large Fermi arc (S_{b1}) of the bottom surface. The black lines and background color indicate the constant energy contours and the strength of orbital weight from the top and bottom atoms. However, when the thickness is thinned down to ten layers, the closed orbit formed by S_{t2} and S_{b1} become less firmly at the transiting area marked by blue dots [see Fig. 4(d)], where electrons transit between S_{t2} and S_{b1} requiring further momentum transfer. This suggests that the WOL orbit will collapse in a thinner system and can be served as a convincing feature of the scenario.

To prove the existence of the WOL orbit, we performed *in situ* dimensionality-dependent tilt experiments. Besides Seg-28, we select three other segments in the same sample with thicknesses of 32, 29, and 26 nm (Seg-32, Seg-29, Seg-26) to conduct quantum oscillation measurements. As an example, Fig. 5(a) plots $d\rho_{xx}/dB$ as a function of $1/B_\perp = 1/(B\cos\theta)$ in Seg-29, where θ is the tilt angle as shown schematically in the inset of Figs. 2(c) and 2(f). A significant feature is discerned that the oscillations depend solely on $B_\perp$, implying a 2D character. This property can be further revealed by the tilt-angle-dependent oscillation frequency F_1, as shown in the inset of Fig. 5(a) [see Fig. S8(a) for more data], where F_1 can be well described by a $1/\cos\theta$ dependence. In comparison, the 3D ellipsoidal Fermi surface shows a notable deviation at $\theta > 50°$. Since we did not perform detailed density functional theory calculations for bulk pockets, we cannot rule out the possibility of a peculiar 3D Fermi surface with even larger k_c/k_a. The angle dependence suggests a 2D transport, which is associated with surface states as demonstrated below by the dimensionality-dependent experiments. Figure 5(b) and Figure S8 show the quantum oscillations $\Delta\rho_{xx}$ for five segments in the same sample with different thicknesses. The corresponding fast Fourier transform (FFT) spectra are shown in Fig. 5(c), where three main oscillation frequencies $F_1 \sim 54$ T, $F_2 = 108$ T, and $F_3 = 148$ T can be seen in the 3D regime. The relatively strong amplitude of F_2 and F_3 in Seg-28 is explained in Sec. IV of the Supplemental Material. Interestingly, we find only $F_2' = 112$ T and $F_3' = 147$ T in Seg-8 [inset of Fig. 5(d)], which are very close to the value of F_2 and F_3 observed in other segments. This signifies that the corresponding oscillation frequencies (F_2 and F_2', F_3, and F_3') originate from the same Fermi surface. Similar values of F_2 and F_3 were previously reported in bulk WTe_2 [52] and $Mo_xW_{1-x}Te_2$ [35], and they were ascribed to bulk hole and electron pocket. Combined with our multicarrier fitting (see Sec. III and Fig. S7 of the Supplemental Material [31]) and band structure calculations [Figs. 4(c) and 4(d)], we conclude that F_2 (F_2') and F_3 (F_3') come from bulk hole and electron pocket, respectively. However, the most prominent oscillation

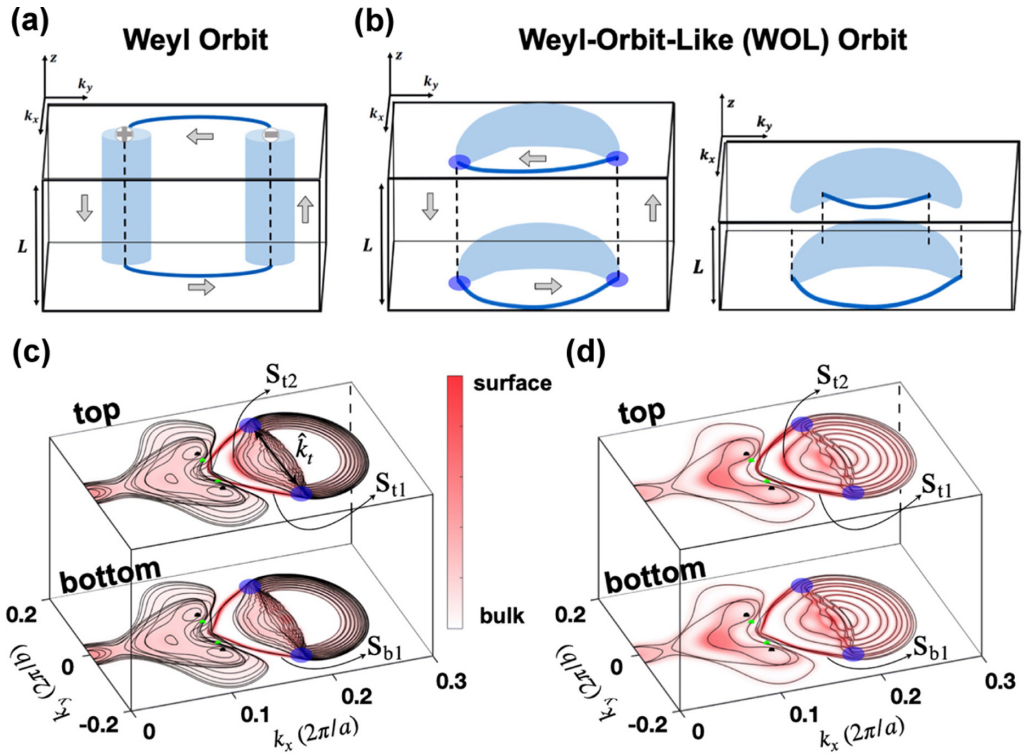

FIG. 4. Schematic figure of Weyl-orbit-like orbit and Fermi surface contours of 30-layer and 10-layer $Mo_{0.25}W_{0.75}Te_2$. (a) The conventional Weyl orbit formed by the Fermi arcs and Landau levels of Weyl points. (b) The Weyl-orbit-like (WOL) orbit consists of unique surface states in a thick (left) and a thin (right) sample. Calculated Fermi surface contours and orbital weight of top and bottom atoms in (c) 30-layer and (d) 10-layer $Mo_{0.25}W_{0.75}Te_2$. In (c) and (d), the constant energy contours and magnitude of orbital weight are indicated by the black lines and the background gradient color. Two major surface states on the top surface are indicated as S_{t1} and S_{t2}, and the major surface states on the bottom surface are indicated as S_{b1}. The original Fermi arc wave vector k_w considered in the conventional Weyl orbit is substituted by k_t in the WOL scenario.

frequency F_1 is missed in Seg-8, indicating that it is a unique property of the 3D sample. The disappearance of F_1 in the 2D sample is consistent with our theoretical calculations that the oscillation induced by S_{t2} and S_{b1} will degrade in thinner samples.

Moreover, Eq. (5) tells us that an extra phase shift induced by sample thickness (L) and tilt-angle-dependent terms ($\vec{k}_w \cdot \hat{B}$ and $2\frac{\mu}{v_\parallel}$) should be observed if Weyl orbit exists, which is distinctly different from conventional Shubnikov–de Haas oscillations [52]. Li [17], Zhang [50], and Galletti [51] have recently conducted thickness-dependent experiments on Weyl orbit. However, the theoretically proposed thickness-dependent phase shift has not yet been observed. Here, we show thickness-dependent phase shift $\phi(L)$ results originating from the WOL orbit (see Sec. V in the Supplemental Material [31] for discussion of tilt-angle-dependent terms). From Fig. 5(b), we can see the phase shift strongly depends on the sample thickness L, which is further corroborated by the Landau-fan diagram shown in Fig. 5(d). The least-square fitting (colored dashed lines) leads to the intercept of 4.29, 3.75, and 3.17 for Seg-32, Seg-29, and Seg-26, respectively. These noninteger or non-half-integer phase shifts cannot be explained by considering topological surface states with the π Berry phase [53–55] or other symmetry contribution of phase terms [56–58] (see Sec. V in the Supplemental Material [31]). If the phase shift comes from Weyl orbit, the sample thickness calculated with Eq. (5) should be consistent with our atomic force microscope (AFM) measurement result. In our case, the orbit is not formed by typical Fermi arcs, thus $\vec{k}_w$ in Eq. (5) should be replaced by the vector $\vec{k}_t$ connecting two blue dots shown in Fig. 4(c). By inserting $\vec{k}_t \cdot \hat{B} = 0$ ($\vec{k}_t$ is in the x-y plane), $\mu = 0.101$ eV, and $v_\parallel = \frac{\hbar \tilde{k}_c}{m^*} = 3.65 \times 10^5$ m/s (see Table S2 and Sec. V in the Supplemental Material [31]) into Eq. (5), the corresponding thicknesses are estimated to be 32, 28, and 24 nm for Seg-32, Seg-29, and Seg-26, respectively. The good agreement between the calculated values and the AFM measurement results suggests the existence of WOL orbit. It should be noted that the different assignment of Landau index n may lead to different calculation results of thickness. Nevertheless, the difference of the phase shift $\Delta\phi(L)$ in the three segments is independent of n. The thickness difference calculated from $\Delta\phi(L)$ is 4 nm, consistent with 3 nm determined by the AFM measurement. We further calculate the frequency of Weyl orbit via the theoretical formula [27],

$$F_s = \frac{\hbar S_k}{2\pi e}. \tag{6}$$

We find the calculated value of S_k from experiment results is in agreement with the theoretical value of $S'_k \sim 10^{-3}$ Å^{-2}, which excludes the possibility of the orbit formed by S_{t1} and S_{b1} ($\sim 10^{-5}$ Å^{-2}). The above discussion shows that the quantum oscillation frequency F_1 is dimensionality dependent,

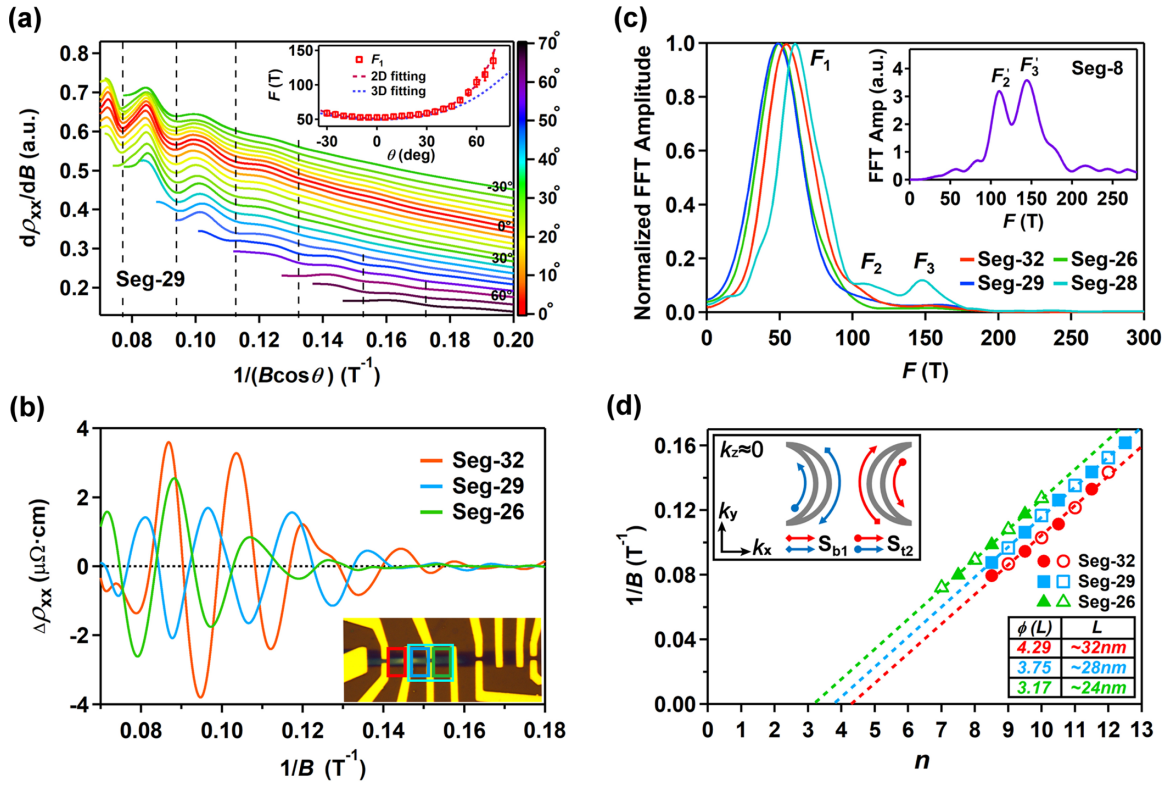

FIG. 5. Signature of Weyl orbit observed in the $Mo_{0.25}W_{0.75}Te_2$ sample. (a) $d\rho_{xx}/dB$ versus $1/B_\perp = 1/(B\cos\theta)$ at different tilt angles. All curves are vertically shifted for clarity and curves with large θ ($>45^\circ$) are horizontally shifted to compensate the additional phase shift (see Sec. V of the Supplemental Material [31]). Vertical dashed lines emphasize the positions of minima of quantum oscillations. The inset shows the angle dependence of FFT frequency F_1. The red and blue dashed lines are the fitting results of the 2D surface states ($1/\cos\theta$) and the 3D ellipsoidal Fermi surface (with $k_c/k_a \sim 3$), respectively. (b) The pronounced quantum oscillations extracted from ρ_{xx} by subtracting a smooth background for $B \parallel c$ ($\theta = 0^\circ$) at 0.3 K. The inset is the optical image of different segments with Seg-32 (red), Seg-29 (blue), and Seg-26 (green). Seg-28 (cyan) is composed of Seg-29 and Seg-26. (c) Fast Fourier transform (FFT) spectra obtained from quantum oscillations shown in (b) at different segments. Seg-28 data is calculated from oscillations shown in Fig. S8. F_1, F_2, and F_3 represent three main oscillation frequencies. The inset shows the FFT of quantum oscillations in Seg-8 at 0.3 K. Only two main oscillation frequencies of F_2' and F_3' are observed. (d) Landau-fan diagram for quantum oscillations $\Delta\rho_{xx}(B)$ measured at 0.3 K and $\theta = 0^\circ$. The least-square fitting gives the intercepts of different segments, which are listed in the inset table with the calculated thickness. The left upper inset shows the new Weyl orbit in $Mo_{0.25}W_{0.75}Te_2$.

which has additional tilt-angle and thickness-dependent phase shift characteristics. All of these features are well consistent with our theoretical calculations of a new kind of Weyl orbit, which extends the generality of Weyl orbit.

III. DISCUSSION

The observations of dimensionality-dependent anisotropic negative MR and an additional quantum oscillation with thickness-dependent phase shift in $Mo_{0.25}W_{0.75}Te_2$ are strong evidences of a type-II WSM with topological surface states. Though our thorough analysis of anisotropic negative MR is consistent with theoretical expectations of a type-II WSM, we have to rule out other possible mechanisms of negative MR, such as current jetting, Knudsen effect, and orbital effect (see Secs. VI and VII in the Supplemental Material [31] for details). The difference of magnetoconductivity between $B_{in} \parallel a$ and $B_{in} \parallel b$ exhibiting a power-law behavior of B^2, which cannot be explained by current jetting, Knudsen effect, and orbital effect, is the key character of chiral anomaly. On the other hand, if the new quantum oscillation comes from Klein tunneling [15], its oscillation frequency should be equivalent to the difference between bulk electron (F_3) and hole (F_2) oscillation frequency. The large discrepancy between $F_1 = 56$ T and $\Delta F = F_3 - F_2 = 40$ T rules out the possibility of Klein tunneling. Furthermore, our controlled experiments on samples with smooth surface (see Fig. S11 of the Supplemental Material [31]) show similar behaviors as that observed on the wedge sample $Mo_{0.25}W_{0.75}Te_2$, demonstrating that the dimensionality dependence of chiral anomaly and quantum oscillations are reproducible and reliable. We note that the unique thickness-dependent phase shift cannot be understood by considering oscillations just from surface states, which only introduces 0 or π Berry phase with the consideration of symmetry and spin-orbit coupling [56–58] in $Mo_{0.25}W_{0.75}Te_2$. Therefore, combining our experimental data and theoretical calculations, it is reasonable to ascribe the extra oscillation frequency F_1 to WOL orbit.

In conclusion, we have prepared $Mo_{0.25}W_{0.75}Te_2$ films with thickness gradient via a CVD method. Using an as-grown sample across 2D and 3D regimes, our systematic low-temperature magnetotransport experiments and

theoretical investigations have shown strong evidences of a type-II WSM with topological surface states. The following two characteristics, including (1) a dimensionality-dependent anisotropic magnetoconductivity enhancement proportional to B_{in}^2 in the configuration of $B_{\text{in}} \parallel E \parallel a$; and (2) an additional dimensionality-dependent quantum oscillation with thickness-dependent phase shift, serve as convincing evidences for chiral anomaly and the new Weyl orbit, respectively. Our *in situ* dimensionality-tuned transport experiment demonstrates an alternative method to search for type-II WSMs, which further deepens the understanding of Fermi arc surface states and topological matters.

ACKNOWLEDGMENTS

We thank Xiaoxiong Liu, Zhijun Wang, and Haizhou Lu for helpful discussions. This work has been supported by the National Basic Research Program of China from the MOST under Grants No. 2016YFA0300601 and No. 2015CB921402; by the National Natural Science Foundation of China under Grants No. 11527806 and No. 11874406; by the Beijing Municipal Science & Technology Commission of China under Grant No. Z191100007219008; by Beijing Academy of Quantum Information Sciences under Grant No. Y18G08; by the Strategic Priority Research Program of the Chinese Academy of Sciences under Grant No. XDB33010300; and by the Synergic Extreme Condition User Facility. Research in Singapore was financially supported by MOE Tier 1 Grant No. RG4/17, MOE Tier 2 Grant No. MOE2016-T2-1-131, and Singapore National Research Foundation under NRF Award No. NRF-NRFF2013-08. This research was supported by the Singapore Ministry of Education under its Tier 2 MOE2017-T2-2-136, Tier 3 MOE2018-T3-1-002, and by the National Research Foundation under its Singapore program NRF-CRP21-2018-0007 and NRF-CRP22-2019-0060. H.L. acknowledges the support by the Ministry of Science and Technology (MOST) in Taiwan under Grant No. MOST 109-2112-M-001-014-MY3.

[1] N. P. Armitage, E. J. Mele, and A. Vishwanath, Weyl and Dirac semimetals in three-dimensional solids, Rev. Mod. Phys. **90**, 015001 (2018).

[2] X. Wan, A. M. Turner, A. Vishwanath, and S. Y. Savrasov, Topological semimetal and Fermi-arc surface states in the electronic structure of pyrochlore iridates, Phys. Rev. B **83**, 205101 (2011).

[3] P. Hosur and X. Qi, Recent developments in transport phenomena in Weyl semimetals, C. R. Phys. **14**, 857 (2013).

[4] S. Huang, S. Xu, I. Belopolski, C. Lee, G. Chang, B. Wang, N. Alidoust, G. Bian, M. Neupane, C. Zhang *et al.*, A Weyl fermion semimetal with surface Fermi arcs in the transition metal monopnictide TaAs class, Nat. Commun. **6**, 7373 (2015).

[5] S. Xu, I. Belopolski, N. Alidoust, M. Neupane, G. Bian, C. Zhang, R. Sankar, G. Chang, Z. Yuan, C. Lee *et al.*, Discovery of a Weyl fermion semimetal and topological Fermi arcs, Science **349**, 613 (2015).

[6] H. Weng, C. Fang, Z. Fang, B. A. Bernevig, and X. Dai, Weyl Semimetal Phase in Noncentrosymmetric Transition-Metal Monophosphides, Phys. Rev. X **5**, 011029 (2015).

[7] B. Q. Lv, H. M. Weng, B. B. Fu, X. P. Wang, H. Miao, J. Ma, P. Richard, X. C. Huang, L. X. Zhao, G. F. Chen *et al.*, Experimental Discovery of Weyl Semimetal TaAs, Phys. Rev. X **5**, 031013 (2015).

[8] X. Huang, L. Zhao, Y. Long, P. Wang, D. Chen, Z. Yang, H. Liang, M. Xue, H. Weng, Z. Fang *et al.*, Observation of the Chiral-Anomaly-Induced Negative Magnetoresistance in 3D Weyl Semimetal TaAs, Phys. Rev. X **5**, 031023 (2015).

[9] C. Zhang, S. Xu, I. Belopolski, Z. Yuan, Z. Lin, B. Tong, G. Bian, N. Alidoust, C. Lee, S. Huang *et al.*, Signatures of the Adler-Bell-Jackiw chiral anomaly in a Weyl fermion semimetal, Nat. Commun. **7**, 10735 (2016).

[10] H. B. Nielsen and M. Ninomiya, The Adler-Bell-Jackiw anomaly and Weyl fermions in a crystal, Phys. Lett. B **130**, 389 (1983).

[11] D. T. Son and B. Z. Spivak, Chiral anomaly and classical negative magnetoresistance of Weyl metals, Phys. Rev. B **88**, 104412 (2013).

[12] A. A. Soluyanov, D. Gresch, Z. Wang, Q. Wu, M. Troyer, X. Dai, and B. A. Bernevig, Type-II Weyl semimetals, Nature (London) **527**, 495 (2015).

[13] F. Y. Bruno, A. Tamai, Q. S. Wu, I. Cucchi, C. Barreteau, A. de la Torre, S. McKeown Walker, S. Riccò, Z. Wang, T. K. Kim *et al.*, Observation of large topologically trivial Fermi arcs in the candidate type-II Weyl semimetal WTe_2, Phys. Rev. B **94**, 121112(R) (2016).

[14] Z. Wang, D. Gresch, A. A. Soluyanov, W. Xie, S. Kushwaha, X. Dai, M. Troyer, R. J. Cava, and B. A. Bernevig, $MoTe_2$: A Type-II Weyl Topological Metal, Phys. Rev. Lett **117**, 056805 (2016).

[15] T. E. OBrien, M. Diez, and C. W. J. Beenakker, Magnetic Breakdown and Klein Tunneling in a Type-II Weyl Semimetal, Phys. Rev. Lett. **116**, 236401 (2016).

[16] Y. Wang, E. Liu, H. Liu, Y. Pan, L. Zhang, J. Zeng, Y. Fu, M. Wang, K. Xu, Z. Huang *et al.*, Gate-tunable negative longitudinal magnetoresistance in the predicted type-II Weyl semimetal WTe_2, Nat. Commun. **7**, 13142 (2016).

[17] P. Li, Y. Wen, X. He, Q. Zhang, C. Xia, Z. Yu, S. A. Yang, Z. Zhu, H. N. Alshareef, and X. Zhang, Evidence for topological type-II Weyl semimetal WTe_2, Nat. Commun. **8**, 2150 (2017).

[18] I. Belopolski, S. Y. Xu, Y. Ishida, X. Pan, P. Yu, D. S. Sanchez, H. Zheng, M. Neupane, N. Alidoust, G. Chang *et al.*, Fermi arc electronic structure and Chern numbers in the type-II Weyl semimetal candidate $Mo_xW_{1-x}Te_2$, Phys. Rev. B **94**, 085127 (2016).

[19] T. Chang, S. Xu, G. Chang, C. Lee, S. Huang, B. Wang, G. Bian, H. Zheng, D. S. Sanchez, I. Belopolski *et al.*, Prediction of an arc-tunable Weyl fermion metallic state in $Mo_xW_{1-x}Te_2$, Nat. Commun. **7**, 10639 (2016).

[20] I. Belopolski, D. S. Sanchez, Y. Ishida, X. Pan, P. Yu, S. Xu, G. Chang, T. Chang, H. Zheng, N. Alidoust *et al.*, Discovery of a new type of topological Weyl fermion semimetal state in $Mo_xW_{1-x}Te_2$, Nat. Commun. **7**, 13643 (2016).

[21] F. Arnold, C. Shekhar, S. Wu, Y. Sun, R. D. d. Reis, N. Kumar, M. Naumann, M. O. Ajeesh, M. Schmidt, A. G. Grushin

et al., Negative magnetoresistance without well-defined chirality in the Weyl semimetal TaP, Nat. Commun. **7**, 11615 (2016).

[22] R. D. d. Reis, M. O. Ajeesh, N. Kumar, F. Arnold, C. Shekhar, M. Naumann, M. Schmidt, M. Nicklas, and E. Hassinger, On the search for the chiral anomaly in Weyl semimetals: The negative longitudinal magnetoresistance, New. J. Phys. **18**, 085006 (2016).

[23] T. J. Thornton, M. L. Roukes, A. Scherer, and B. P. Van de Gaag, Boundary Scattering in Quantum Wires, Phys. Rev. Lett. **63**, 2128 (1989).

[24] M. J. M. de Jong and L. W. Molenkamp, Hydrodynamic electron flow in high-mobility wires, Phys. Rev. B **51**, 13389 (1995).

[25] P. J. W. Moll, N. L. Nair, T. Helm, A. C. Potter, I. Kimchi, A. Vishwanath, and J. G. Analytis, Transport evidence for Fermi-arc-mediated chirality transfer in the Dirac semimetal Cd_3As_2, Nature (London) **535**, 266 (2016).

[26] A. C. Potter, I. Kimchi, and A. Vishwanath, Quantum oscillations from surface Fermi arcs in Weyl and Dirac semimetals, Nat. Commun. **5**, 5161 (2014).

[27] Y. Zhang, D. Bulmash, P. Hosur, A. C. Potter, and A. Vishwanath, Quantum oscillations from generic surface Fermi arcs and bulk chiral modes in Weyl semimetals, Sci. Rep. **6**, 23741 (2016).

[28] W. E. Liu, E. M. Hankiewicz, and D. Culcer, Quantum transport in Weyl semimetal thin films in the presence of spin-orbit coupled impurities, Phys. Rev. B **96**, 045307 (2017).

[29] S. Murakami and S. I. Kuga, Universal phase diagrams for the quantum spin Hall systems, Phys. Rev. B **78**, 165313 (2008).

[30] J. Zhou, J. Lin, X. Huang, Y. Zhou, Y. Chen, J. Xia, H. Wang, Y. Xie, H. Yu, J. Lei *et al.*, A library of atomically thin metal chalcogenides, Nature (London) **556**, 355 (2018).

[31] See Supplemental Material at http://link.aps.org/supplemental/10.1103/PhysRevB.104.085423 for details about band structure calculation, electron-electron interaction analysis, multicarrier transport analysis, quantum oscillation analysis, tilt-angle-dependent phase shift analysis, and negative MR analysis, and which includes Refs. [59–66].

[32] J. Zhou, F. Liu, J. Lin, X. Huang, J. Xia, B. Zhang, Q. Zeng, H. Wang, C. Zhu, L. Niu *et al.*, Large-area and high-quality 2D transition metal telluride, Adv. Mater. **29**, 1603471 (2017).

[33] J. F. Moulder, *Handbook of X-Ray Photoelectron Spectroscopy* (Perkin-Elmer Corp., Physical Electronics Division, Norwalk, 1995), p. 97.

[34] X. Ma, P. Guo, C. Yi, Q. Yu, A. Zhang, J. Ji, Y. Tian, F. Jin, Y. Wang, K. Liu *et al.*, Raman scattering in the transition-metal dichalcogenides of 1T-$MoTe_2$, T_d-$MoTe_2$, and T_d-WTe_2, Phys. Rev. B **94**, 214105 (2016).

[35] D. Fu, X. Pan, Z. Bai, F. Fei, G. A. Umana-Membreno, H. Song, X. Wang, B. Wang, and F. Song, Tuning the electrical transport of type-II Weyl semimetal WTe_2 nanodevices by Mo doping, Nanotechnology **29**, 135705 (2018).

[36] Y. Lv, L. Cao, X. Li, B. Zhang, K. Wang, B. Pang, L. Ma, D. Lin, S. Yao, J. Zhou *et al.*, Recent developments in transport phenomena in Weyl semimetals, Sci. Rep. **7**, 44587 (2017).

[37] N. F. Mott, Conduction in non-crystalline materials, Philos Mag. **19**, 835 (1969).

[38] R. M. Hill, Variable-range hopping, Phys. Status Solidi A. **34**, 601-613 (1976).

[39] M. N. Ali, J. Xiong, S. Flynn, J. Tao, Q. D. Gibson, L. M. Schoop, T. Liang, N. Haldolaarachchige, M. Hirschberger, N. P. Ong, and R. J. Cava, Large, non-saturating magnetoresistance in WTe_2, Nature (London) **514**, 205 (2014).

[40] P. A. Lee and T. V. Ramakrishnan, Disordered electronic systems, Rev. Mod. Phys. **57**, 287 (1985).

[41] A. Y. Kuntsevich, L. A. Morgun, and V. M. Pudalov, Electron-electron interaction correction and magnetoresistance in tilted fields in Si-based two-dimensional systems, Phys. Rev. B **87**, 205406 (2013).

[42] Q. Wang, P. Yu, X. Huang, J. Fan, X. Jing, Z. Ji, Z. Liu, G. Liu, C. Yang, and L. Lu, Observation of weak anti-localization and electron-electron interaction on few-layer 1T'-$MoTe_2$ thin films, Chin. Phys. Lett. **35**, 077303 (2018).

[43] S. N. Zhang, Q. S. Wu, Y. Liu, and O. V. Yazyev, Magnetoresistance from Fermi surface topology, Phys. Rev. B **99**, 035142 (2019).

[44] J. M. Ziman, *Electrons and Phonons: The Theory of Transport Phenomena in Solids* (Oxford University Press, New York, 2001).

[45] A. A. Kozikov, A. K. Savchenko, B. N. Narozhny, and A. V. Shytov, Electron-electron interactions in the conductivity of graphene, Phys. Rev. B **82**, 075424 (2010).

[46] B. Jouault, B. Jabakhanji, N. Camara, W. Desrat, C. Consejo, and J. Camassel, Interplay between interferences and electron-electron interactions in epitaxial graphene, Phys. Rev. B **83**, 195417 (2011).

[47] H. Z. Lu and S. Q. Shen, Weak antilocalization and localization in disordered and interacting Weyl semimetals, Phys. Rev. B **92**, 035203 (2015).

[48] C. M. Wang, H. P. Sun, H. Z. Lu, and X. C. Xie, 3D Quantum Hall Effect of Fermi Arcs in Topological Semimetals, Phys. Rev. Lett. **119**, 136806 (2017).

[49] C. Zhang, A. Narayan, S. Lu, J. Zhang, H. Zhang, Z. Ni, X. Yuan, Y. Liu, J. Park, E. Zhang *et al.*, Evolution of Weyl orbit and quantum Hall effect in Dirac semimetal Cd_3As_2, Nat. Commun. **8**, 1272 (2017).

[50] C. Zhang, Y. Zhang, X. Yuan, S. Lu, J. Zhang, A. Narayan, Y. Liu, H. Zhang, Z. Ni, R. Liu *et al.*, Quantum Hall effect based on Weyl orbits in Cd_3As_2, Nature (London) **565**, 331 (2019).

[51] L. Galletti, T. Schumann, D. A. Kealhofer, M. Goyal, and S. Stemmer, Absence of signatures of Weyl orbits in the thickness dependence of quantum transport in cadmium arsenide, Phys. Rev. B **99**, 201401(R) (2019).

[52] Z. Zhu, X. Lin, J. Liu, B. Fauque, Q. Tao, C. Yang, Y. Shi, and K. Behnia, Quantum Oscillations, Thermoelectric Coefficients, and the Fermi Surface of Semimetallic WTe_2, Phys. Rev. Lett. **114**, 176601 (2015).

[53] Y. Ando, Topological insulator materials, J. Phys. Soc. Jpn. **82**, 102001 (2013).

[54] J. Hu, J. Y. Liu, D. Graf, S. M. A. Radmanesh, D. J. Adams, A. Chuang, Y. Wang, I. Chiorescu, J. Wei, L. Spinu, and Z. Q. Mao, Pi Berry phase and Zeeman splitting of Weyl semimetal TaP, Sci. Rep. **6**, 18674 (2016).

[55] P. Sergelius, J. Gooth, S. Bäßler, R. Zierold, C. Wiegand, A. Niemann, H. Reith, C. Shekhar, C. Felser, B. Yan, and K. Nielsch, Berry phase and band structure analysis of the Weyl semimetal NbP, Sci. Rep. **6**, 33859 (2016).

[56] A. Alexandradinata and L. Glazman, Geometric Phase and Orbital Moment in Quantization Rules for Magnetic Breakdown, Phys. Rev. Lett. **119**, 256601 (2017).

[57] A. Alexandradinata, C. Wang, W. H. Duan, and L. Glazman, Revealing the Topology of Fermi-Surface Wave Functions from Magnetic Quantum Oscillations, Phys. Rev. X **8**, 011027 (2018).

[58] A. Alexandradinata and L. Glazman, Semiclassical theory of Landau levels and magnetic breakdown in topological metals, Phys. Rev. B **97**, 144422 (2018).

[59] L. Wu and M. Guidry, The ground state of monolayer graphene in a strong magnetic field, Sci. Rep. **6**, 22423 (2016).

[60] Y. Lin, C. Dimitrakopoulos, D. B. Farmer, S. Han, Y. Wu, W. Zhu, D. K. Gaskill, J. L. Tedesco, R. L. Myers-Ward, C. R. Eddy, Jr. *et al.*, Multicarrier transport in epitaxial multilayer graphene, Appl. Phys. Lett. **97**, 112107 (2010).

[61] D. Shoenberg, *Magnetic Oscillations in Metals* (Cambridge University Press, Cambridge, UK, 1984).

[62] L. Ritchie, G. Xiao, Y. Ji, T. Y. Chen, C. L. Chien, M. Zhang, J. Chen, Z. Liu, G. Wu, and X. X. Zhang, Magnetic, structural, and transport properties of the Heusler alloys Co_2MnSi and NiMnSb, Phys. Rev. B **68**, 104430 (2003).

[63] S. Hikami, A. I. Larkin, and Y. Nagaoka, Spin-orbit interaction and magnetoresistance in the two dimensional random system, Prog. Theor. Phys. **63**, 707 (1980).

[64] A. B. Pippard, *Magnetoresistance in Metals* (Cambridge University Press, Cambridge, UK, 1989).

[65] H. M. Rosenberg, *Low Temperature Solid State Physics* (Oxford University Press, New York, 1963).

[66] D. Rhodes, R. Schönemann, N. Aryal, Q. Zhou, Q. R. Zhang, E. Kampert, Y.-C Chiu, Y. Lai, Y. Shimura, G. T. McCandless *et al.*, Bulk Fermi surface of the Weyl type-II semimetallic candidate γ-$MoTe_2$, Phys. Rev. B **96**, 165134 (2017).